processes

MDPI

Article

Comparison of Glass–Glass versus Glass–Backsheet Encapsulation Applied to Carbon-Based Perovskite Solar Cells

Nikoleta Kyranaki [1,*], Lara Perrin [2], Lionel Flandin [2], Emilie Planès [2], Cynthia Farha [2], Lukas Wagner [3], Karima Saddedine [3], David Martineau [4] and Stéphane Cros [1]

1 Université Grenoble Alpes, CEA, Liten, Campus Ines, 73375 Le Bourget du Lac, France; stephane.cros@cea.fr
2 University Grenoble Alpes, University Savoie Mont Blanc, CNRS, Grenoble INP, LEPMI, 38000 Grenoble, France; lara.perrin@univ-smb.fr (L.P.); lionel.flandin@univ-smb.fr (L.F.); emilie.planes@univ-smb.fr (E.P.); cynthia_f_8@hotmail.co.uk (C.F.)
3 Fraunhofer Institute for Solar Energy Systems ISE, Heidenhofstraße 2, 79110 Freiburg, Germany; lukas.wagner@physik.uni-marburg.de (L.W.); karima.saddedine@web.de (K.S.)
4 Solaronix S.A., Rue de l'Ouriette 129, 1170 Aubonne, Switzerland; david.martineau@solaronix.com
* Correspondence: nikolkiranaki@gmail.com

Abstract: The record photovoltaic performance of perovskite solar cells is constantly increasing, reaching 26% currently. However, there is a crucial need for the development of simple architectures that are compatible with large-scale industrialization and possess adequate stability. The aim of the work presented here is to compare the efficiency of glass–glass and glass–backsheet encapsulations for carbon-based perovskite solar cell application, which possesses a great potential for industrialization. This was conducted by first separating the relative effects of humidity and heat. A time evolution of the macroscopic power conversion efficiency (PCE) was performed, together with specific characterizations in order to scout the origin of flaws and degradations. A significant contribution of the paper is the identification of both TiO_2 and carbon layers as barriers against moisture permeation, which inhibit moisture paths through the interfaces. This is the origin of the equivalent durability of both studied systems, even if the glass–backsheet encapsulation was found to be less efficient than the glass–glass encapsulation at protecting perovskite from damp-heat aging when TiO_2 or carbon layers are not used.

Keywords: photovoltaics; perovskite; encapsulation process; durability

Citation: Kyranaki, N.; Perrin, L.; Flandin, L.; Planès, E.; Farha, C.; Wagner, L.; Saddedine, K.; Martineau, D.; Cros, S. Comparison of Glass–Glass versus Glass–Backsheet Encapsulation Applied to Carbon-Based Perovskite Solar Cells. *Processes* **2023**, *11*, 2742. https://doi.org/10.3390/pr11092742

Academic Editors: Ioannis Spanopoulos and Martina Schmid

Received: 26 July 2023
Revised: 30 August 2023
Accepted: 11 September 2023
Published: 14 September 2023

1. Introduction

The power conversion efficiency (PCE) of perovskite solar cells is rising steadily and now reaches 26% [1], which represents a threefold increase over 10 years [2]. To attain such an efficiency achievement, the various layers constituting the device architecture have been continuously improved [3,4]. Unfortunately, the stability/reliability of perovskite devices still needs progress [5]. In other words, further research should be carried out to ensure that perovskite devices maintain stable electrical parameters during J–V curve measurement and are able to pass the ISOS or IEC standards. Although prolonged durability has already been achieved for some device architectures [6,7], the exact contribution of each component toward better reliability and the occurring degradation mechanisms both need to be well understood to make the adequate choice of material combination.

A promising first solution is the use of device architectures without any hole transporting material (HTM), and especially without organic materials. For instance, the major part of highly efficient perovskite architectures uses the costly hole transporting Spiro-OMeTAD material, which is known to be unstable at high temperatures [8]. The proposed solution is affordable due to the availability of carbon-based perovskite solar cells (c-PSC). Various c-PSC device architectures have already been tested [9], providing stable, cheap and large-scale processable perovskite devices. We can bring to light two recent works

conducted by our teams. A record efficiency of 18.5% was achieved in 2022 by Zouhair et al. [10] by adding a 2D perovskite electron blocking layer between the 3D perovskite absorber and the carbon electrode. Another promising performance enhancement was also described in 2023 by Perrin et al. [11] leading to a 14% efficiency for a fully scalable architecture using inkjet printing for the perovskite deposition together with a process fully conducted in ambient atmosphere. The perovskite deposition is here made as a final step via infiltration through a ZrO_2/carbon mesoporous scaffold without any HTM. The latter technology presenting a particular interest for industrial scale-up will be used in this paper. The different layers of the selected c-PSC device are inorganic, thus more robust than organic materials. According to the literature [12–14], TiO_2, ZrO_2 and FTO are thermally stable and highly corrosion-resistant materials. In addition, the carbon electrode is noted for its chemical stability and hydrophobicity [15], the latter providing additional protective properties [16] under environmental stresses.

The literature reveals that the choice of perovskite absorber is also crucial for the heat and moisture resistance of the photovoltaic devices [17]. The perovskite absorber used here is a ($MAPbI_3$), $(AVAI)_{0.05}$ formulation. The ammonium valeric acid iodide (AVAI) additive was added to the traditional methyl ammonium lead iodide ($MAPbI_3$) perovskite formulation for the achievement of better durability against humidity and temperature [16]. Thermal decomposition of $MAPbI_3$ perovskite into PbI_2 could occur under prolonged thermal stress conditions as low as 85 °C [17]. In addition, the presence of humidity in perovskite materials has been identified as tragic. $MAPbI_3$ experiences hydrolysis, which is thermally accelerated. First, water molecules are attached to the grain boundaries of the perovskite layer, creating a monohydrate and/or dihydrate phase. Then, when the layer is heated, the intermediate phase decomposes with lead iodide (PbI_2) as a byproduct [18].

For the reasons mentioned above, AVAI additive was added to extend the service life of perovskite [6] in our systems. However, the use of an efficient encapsulation [19] is mandatory to obtain a reasonable lifetime under the so-called damp-heat (DH) test (85 °C/85% RH). The different encapsulation concepts usually applied to perovskite photovoltaic devices are the following: glass–glass encapsulation using various polymers as sealant material (e.g., polyolefin elastomer, ethylene vinyl acetate, polyurethane, polyisobutylene [20,21] or UV-cured epoxies and resins [21,22]), glass frit sealing [23] or a single polymer rear cover (for instance: poly methyl methacrylate [24], fluoropolymer [25], etc.). More specifically, Fu et al. [20] found that polyurethane may be applied at a low lamination temperature (80 °C), but encapsulated cells of similar architecture to those studied here withstood 325 h of testing at 85 °C. Otherwise, Shi et al. [21] utilized blanket polyisobutylene as an encapsulant with promising results (540 h of DH 85 °C/85% RH stability), but the specific material can only be used as an edge-sealant in case of large-area PV modules. Cao et al. [22] sealed devices with UV resin, however, the devices were not tested at high relative humidity and, in general, the selection of a UV resin should be conducted carefully since some of them are incompatible with the perovskite devices when applied as encapsulants and do not provide thorough protection when applied only as sealants. Additionally, Martins et al. [23] suggested laser-assisted glass–frit encapsulation, but the concept is not commercially mature and was only tested at low temperatures (20 °C), which cannot cause any serious moisture ingress. Finally, poly methyl methacrylate (PMMA) [24] and fluoropolymer [25] layers were examined as rear covers, with the PMMA not being tested at harsh conditions but the fluoropolymer layers showing promising results (device stability after 175 days under light soaking and 50% RH). Nevertheless, encapsulated perovskite devices proved their great potential for outdoor farm application with a demonstrated conservation of at least 80% of initial performances (T80), during 5832 h, under real operating conditions [26]. However, no general rules can be determined about the best encapsulating materials for perovskite photovoltaic devices as stability issues depend on several parameters: the architecture of the device, formulation of the perovskite, encapsulation type and processing parameters. Some combinations have already proved their potential to be able to maintain at least 80% of the perovskite initial performances

for up to 1000 h at 85 °C/85% RH exposure. The latter mainly use glass–glass encapsulation sealed either using polyolefin [27], ethylene vinyl acetate (EVA) polymer [28] or ionomer [6] together with butyl rubber edge sealant, which can be carried out by already commercially available techniques (lamination). EVA is the encapsulating material mainly used for silicon photovoltaics; however, presents some disadvantages: degradation under UV light, relatively low ion resistivity responsible for the acceleration of potential induced degradation, and the production of acetic acid as a result of hydrolysis. The latter drawback is highly detrimental to perovskite durability. For instance, recent papers propose the addition of a primary Kapton encapsulation in order to reduce the impact of the acetic acid released by the EVA during the panels' lamination and operation on perovskite device performance [26]. In addition, EVA needs a cross-linking stage during lamination, leading to increased lamination times and temperatures. The sealing material of choice for the present work will thus be an ionomer possessing a lower Water Vapor Transmission Rate (WVTR), higher optical transparence and higher ion resistivity than EVA. Furthermore, ionomers are chemically compatible with perovskite absorbers as they do not produce an acetic acid degradation byproduct [29]. A different polyolefin-based material or polyurethane was not selected due to the extremely low WVTR of the ionomer [30].

If glass–glass sealed encapsulation is largely used and well known for its efficient protection against water, corrosion and abrasion, glass–backsheet using a flexible polymer as a rear cover is also the focus of intense interest. The main advantages of the latter are a lighter weight and better heat dissipation. The literature already explores the comparison between such encapsulation types, but mainly for silicon photovoltaic devices. The identified advantages noted for silicon devices are an increase in water protection and lessened degradation of the encapsulation with time for glass–glass vs. less mechanical constraints and additional current in bifacial modules due to scattering effects for the glass-backsheet [31–33]. It would be interesting to investigate the compatibility of the two types of encapsulation systems, especially in the case of the carbon-based perovskite solar cell architecture, presenting a particular interest for industrial scale-up [34].

The aim of the presented work will thus be to highlight the potential differences between glass–glass and glass–backsheet encapsulations in the protection of the c-PSC recent technology. The research presented here was conducted firstly by analyzing the impact of the encapsulation processes on initial photovoltaic properties, and secondly by separately analyzing the relative effect of humidity and heat. A time evolution of the macroscopic power conversion efficiency (PCE) was performed, together with specific characterizations in order to scout the origin of flaws and degradations: light-beam-induced current mapping, impedance spectroscopy, photoluminescence imaging and a specifically developed image processing technique using partial device aging.

2. Materials and Methods

The carbon-based perovskite solar cells presented in Figure 1 were provided by Solaronix and encapsulated with different systems. Devices were sealed in vacuum bags between fabrication and encapsulation. Their photovoltaic performances were checked to be fully stable on this timeframe. Full-encapsulated photovoltaic devices were then subjected to different aging conditions and characterized during aging.

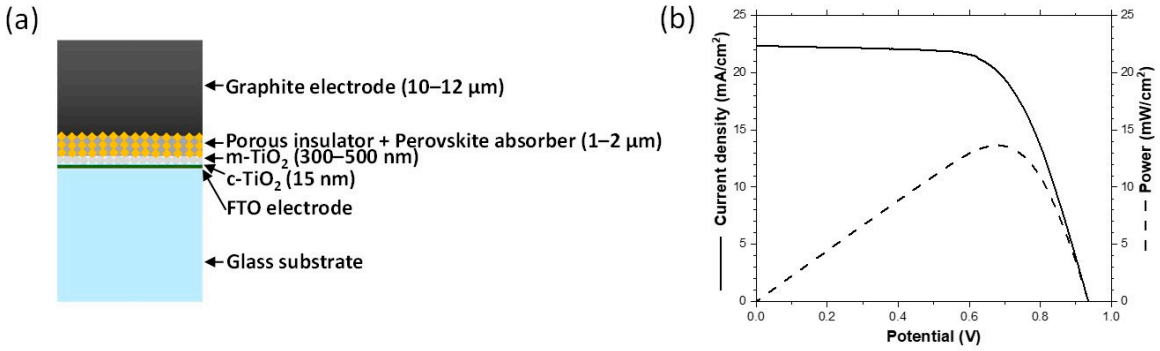

Figure 1. (**a**) Architecture of the studied PV devices (the glass and graphite layers are scaled down in order to represent the proportions of the rest layers correctly); (**b**) typical current–voltage and power–voltage curves for devices before encapsulation.

2.1. Fabrication of the c-PSC Devices

In this work, the active area of c-PSC devices was 1.25 cm × 1.20 cm and devices were manufactured on 5 cm × 5 cm glass substrates in order to allow for a worthy encapsulation. A glass plate with Fluorine-doped tin oxide (FTO) coating from Solaronix, Aubonne, Switzerland, laser-patterned, was washed in an ultrasonic bath. The solvents used were 1% aqueous solution of Hellmanex, acetone and isopropanol. A solution was formed by mixing 75% of titanium diisopropoxide bis (acetylacetonate) in isopropanol (Sigma-Aldrich, St. Louis, MO, USA). The described solution was further mixed in absolute ethanol with proportion 1:80. Spray coating was applied, with oxygen as the carrier, on a plate preheated to 500 °C in order to generate a compact TiO_2 layer of 30–50 nm thickness. The plate with the compact TiO_2 layer was left until it reached room temperature. Then, TiO_2 paste from Solaronix was screen-printed for the development of the mesoporous TiO_2 layer, with thickness 300–500 nm. The described procedure was followed by drying of the sample at 150 °C for 5 min, subsequent heating to 500 °C for 30 min and cooling until reaching room temperature. Afterward, a mesoporous ZrO_2 layer (Solaronix) of thickness 1–2 μm was screen-printed on top of the mesoporous TiO_2 layer and the same drying and sintering method as mentioned above was followed. Finally, the conductive carbon paste (Solaronix) was screen-printed for the formation of a 10–12 μm thick back contact. The sample was again dried, sintered and cooled down as before.

The formula for the perovskite precursor ink was obtained as follows: A mixture of 0.191 g methyl ammonium iodide (MAI, Dyesol, Queanbeyan, NSW, Australia), 0.553 g PbI_2 (TCL Chemicals, Tokyo, Japan) and 0.015 g 5-ammonium valeric acid iodide (5-AVAI, Dyesol) was formed. The described mixture was dissolved in 1 mL of gamma-butyrolactone (GBL, Sigma Aldrich). The sealed solution was stirred at 70 °C for 30 min. Without cooling down, the solution was filtered through a 0.2 μm PTFE filter and left to reach room temperature. The developed ink was inkjet-printed on the electrode stack with a PixDro LP50 inkjet printer (SÜSS MICROTEC SE, Garching, Germany). Annealing of the samples followed at 50 °C for 10 min, followed by humidity-assisted thermal treatment at 40 °C and 75% RH for 135 h, in order to reach their optimal performances.

In addition to photovoltaic full devices, partial devices were also considered to investigate the impact of the different layers on the moisture-induced degradation. The same procedure as above was used, except that the partial devices were made either without the carbon electrode or without the titanium dioxide and carbon electrode.

2.2. Encapsulation of the Photovoltaic Devices

Two encapsulation systems were studied: glass–polymer backsheet and glass–glass. For the encapsulation, an ionomer with a WVTR of 1.9 $g/m^2/day$ @ 38 °C, 95% RH was utilized as the sealing material (thickness = 500 μm). First, the c-PSC devices manufactured on 5 × 5 cm front glass substrates were completed with long silver contacts and ribbons of

adhesive conductive tapes on the last cm in order to be able to measure their photovoltaic properties after encapsulation. Then, either a gas barrier polymer (ETFE) backsheet of 0.203 mm with WVTR < 5×10^{-4} g/m^2/day @ 23 °C, 85% RH or a 1.1 mm thick soda-lime glass lid was used as rear cover. In the case of the glass rear cover, a lack of adhesion was revealed and thus an additional polyisobutylene (PIB) edge sealant of 0.5 cm width was added (see Figure S1). A PIB-including desiccant (solvent and primer free) with WVTR < 0.12 g/m^2/day @ 38 °C, 95% RH was thus used in the final proposed glass–glass encapsulation version. No additional edge sealant was added for the glass–backsheet encapsulation.

The 1.25 × 1.20 cm active devices were manufactured on 5 × 5 cm glass substrates in order to allow for a worthy encapsulation from several points of view: (i) enough space to allow for a more-than-1-cm ionomer sealant strip outside the active area to limit edge permeation, (ii) enough space to be able to keep this 1 cm sealant strip when adding the external ribbon contact to ensure the electrical contact with internal silver contacts, and (iii) enough space to be able to add the 0.5 cm PIB edge sealant.

The described stacks were inserted into an industrially used vacuum laminator, where the samples remained at temperature 130 °C for 10 min. The initial pressure was 1 bar for 3 min, followed by vacuum for the same amount of time. Finally, the samples remained at 1 bar of pressure for the rest of the duration. Prior to lamination, the devices were placed on a sheet of glass and between two layers of non-adhesive paper. The information in the ionomer datasheet accounted for the selection of lamination conditions and no further optimizations were carried out. However, for the glass–glass devices, shims of equal thickness to the stacks were placed around the samples to prevent glass breakage.

For the partial devices also studied, the same encapsulation procedures were applied but no external electrical contacts were applied.

2.3. Aging Campaigns

The samples were placed either in a Clima Temperatur Systeme (CTS, type C-40/100) with environmental chamber at 85 °C/85 RH conditions under air (for DH aging, corresponding to IEC standard conditions for module commercialization) or in a Memmert UNB 100 oven at 85 °C under nitrogen (for T aging). As the oven is under ambient air, the encapsulated devices for T aging were additionally placed inside sealed nitrogen bags to be sure to prevent both oxygen and moisture ingresses. This T aging condition was included to potentially identify the degradation mechanisms at high temperature in the absence of high levels of moisture/oxygen. All aging campaigns were conducted in dark and with the devices in open-circuit condition during 2500 h. Presented PCE data are for J–V tracking of the same samples. To do so, samples were periodically taken out of the chamber. As a general procedure for our solar device aging campaigns, some samples were also aged without being measured at each sampling point, and photovoltaic parameter evolutions were found to be similar to the others. In addition, devices submitted to the full characterization set (imaging and impedance spectroscopy) presented a negligible deviation as compared to others.

2.4. Characterizations

The J–V curves were measured by a Keithley 2602A System source meter while the cells were subjected to 1 sun illumination. The illumination was provided by a Newport 92190–1000 light source and controlled via a Newport 69922 power supply (Newport, CA, USA). The minimum voltage of the J–V scan was −0.3 V, while the maximum was 1.5 V. The J–V curves were measured with a 5 mV step and the increment was 100 ms. Three reverse-forward pairs were recorded to ensure stability. In this work, the final reverse measurement is reported for the evolution of the electrical performance parameters during DH or T aging.

Light-beam-induced current (LBIC) mapping was performed for the investigation of the spatially distributed defects in order to control both the lamination step and the

evolution during aging. LBIC mapping was obtained using a LEPMI home-made system consisting of a laser beam at 532 nm (0.7 mm diameter) and an automated structure holding the laser and scanning the sample surface with resolution 0.4 mm. A Keithley 2400 source meter was utilized in order to maintain the device at short circuit and measure the short circuit current produced by the cell at the incident spot of the beam. The generated current maps were transformed into color scale images using OriginLab software (Origin 2021, 9.8) and processed via ImageJ for the extraction of the statistics of the measurements. It should be mentioned that, due to the laser diameter, a part of the illuminated area was not covered by perovskite when analyzing the last millimeter border, resulting in lower Isc values which should not be taken into account for homogeneity assignment.

Impedance spectroscopy (IS) was applied for the analysis of the evolution of resistive and capacitive effects, within the bulk or the different interfaces of the devices. The impedance spectra were measured using a Bio-Logic SAS SP-300 impedance spectroscopy instrument, while the sample was exposed to 1 sun illumination, provided by an ORIEL LCS-100 solar simulator (Newport, CA, USA). Voltage of 0.7 V was applied to the cell with oscillation of 30 mV. The frequency range was 2 MHz to 0.5 Hz and the number of points was 10 per decade. The obtained Nyquist plots were fitted with a 3-RC model [35] described later in the manuscript in order to calculate the series resistance (Rs), geometrical resistance (Rct), recombination resistance (Rrec) and ideality factor of the first semicircle [35], which is calculated using the following equation [36]:

$$Z_{CPE_1} = \frac{1}{Q_1(i\omega)^{n_1}}$$

where Z_{CPE_1} is the impedance of the constant phase element and n_1 is the ideality factor. The value of Q_1 depends on the ideality factor. If $n_1 = 1$, the constant phase element acts as an ideal capacitor; if $n_1 = 0$, the constant phase element reduces to a real resistor; and if $n_1 = 0.5$, the constant phase element reduces to Warburg element. The described model was fitted via utilization of the Python library impedance [37].

To characterize the absorber quality, photoluminescence (PL) imaging was utilized. The PL images were acquired using a GREATEYES LumiSolarCell Electro- and Photoluminescence Inspection System, including a CCD camera and green LEDs as the light source. The selected current for the light source was 1000 mA. The camera was focused on distance 0.45 m while the aperture opening was f/8. The integration and delay time were 2 s and 1 ms, respectively. A filter of wavelengths below 750 $\pm$ 25 nm was applied in order to filter out artifact illumination not emitted from the cell. Full PV devices were analyzed from the transparent side and in open-circuit condition. The PL images were then processed using the Python Imaging Library Pillow 9.1.0 [38] in order to extract the PL illumination of cells in a grey level scale.

Finally, partial-stack architectures were characterized during aging with the help of a machine learning imaging technique analyzing the variation in color of the full surface of devices. For this purpose, devices without the dark carbon layer were used in order to be able to detect the color related to perovskite. According to the procedure described in CEA's previous works [39,40], images were acquired at different aging times and then an algorithm was applied. It computes the evolution of both the area covered by the perovskite absorber and the thickness of the perovskite absorber by generating a thickness map (here, red color shade scale was used). It is important to precise that given thicknesses values are related to effective thickness of the active (non-significantly degraded) perovskite. Indeed, in our systems, the thickness of the active layer (presented as "porous insulator + perovskite absorber" in Figure 1a) remains constant. After aging, it can, however, be composed of either perovskite and/or its degradation compounds (not absorbing in the same range). As a result, the perovskite layer lightens as it ages, changing from dark brown to light yellow. Thus, the maximum thickness scale corresponding to initial state was normalized to 1 here.

3. Results and Discussions

Figure 1a presents the typical architecture of carbon-based perovskite solar cells (c-PSC) used in this study, i.e., Glass/FTO/TiO_2/ZrO_2 + PK/carbon. The mesoporous insulating layer in ZrO_2 acts as a host for the infiltrated perovskite active material. As detailed in the experimental section, all layers constituting the device architecture can be realized by either spray or screen-printing techniques that are compatible with large-surface devices. For the perovskite infiltration, inkjet printing was used in order to stay compatible with the development and industrialization of large-area perovskite devices [11]. The different photovoltaic parameters obtained for a batch of 18 non-encapsulated cells are presented in Table 1 (Figure 1b presenting typical J–V and P–V obtained curves).

Table 1. Photovoltaic parameters for devices before encapsulation (typical 18-cell batch).

18 Cells Batch	PCE (%)	Jsc (mA/cm^2)	Voc (V)	FF
Average value	13.26	22.60	0.927	0.63
Standard deviation	±0.64	±0.59	±0.007	±0.02

3.1. Impact of the Lamination Processes on c-PSC Devices

Figure 2a presents the typical architecture of our encapsulated photovoltaic (PV) devices. Two encapsulation systems were studied: glass front substrate–polymer backsheet and glass front substrate–glass rear cover, both sealed using a laminated ionomer. The two encapsulation systems are illustrated via photographs of the devices in Figure 2b, and the different steps of the encapsulation process are detailed in Figure S1 in the Supplementary Materials File.

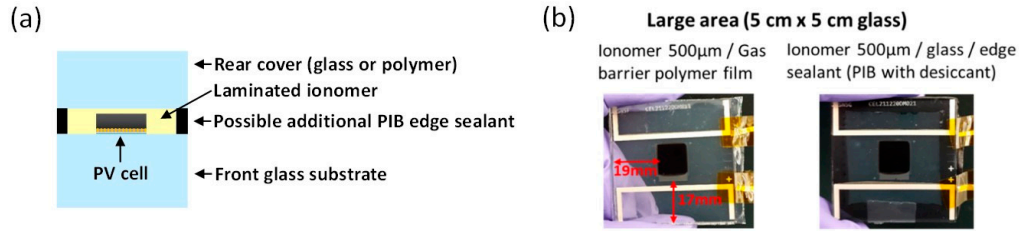

Figure 2. (**a**) Architecture of the encapsulated PV devices; (**b**) photographs of the 2 encapsulation combinations here selected.

First, glass–glass encapsulation was performed, which rapidly highlighted the problem of the adhesion of the ionomer sealing material (see photographs in Figure S2a in Supplementary Materials showing evidence of water fog penetration during 85 °C/85% RH aging). This was together confirmed via a rapid loss of performance during aging, as illustrated in Figure S2b in Supplementary Materials with a 40% loss of performance after 300 h and a 90% loss after 600 h (based on Jsc degradation). According to the literature [29], the adhesion of ionomers to glass has been shown to be less effective than the traditional EVA mainly used for silicon device glass–glass sealing. This could lead to delamination after a short period. In addition, glass warping could occur due to the difference in temperature when introducing the cold PV device within the preheated laminator [41]. This may accentuate the resulting bad adhesion of glass–glass encapsulation. In the case of glass–backsheet encapsulation, such behavior was not observed, and the sealing seemed to be of good quality as the flexible polymer backsheet was able to take the shape of both areas (i.e., filled or not filled by the PV stack). In order to fix the problem encountered in glass–glass encapsulation, an additional 0.5 cm edge layer of polyisobutylene sealant (initial thickness 1.2 mm, before melting) was added (as illustrated in Figures 2 and S1).

Figure 3 presents the impact of the final selected encapsulating systems "glass/ionomer/backsheet" and "glass/ionomer + PIB/glass" on photovoltaic performances (see Figure S3 in Supplementary Materials for the impact on the J–V curves). Both systems seemed

to have an impact on the initial properties, with a relative reduction of the conversion efficiency (PCE) of about 20–25%, giving PCE values of around 9–10% for devices right after encapsulation. For other PV parameters, glass–backsheet encapsulation seems to affect the Jsc less but the FF more, ultimately producing a quite equivalent PCE that is, however, slightly better for the glass–backsheet process. The Voc value is impacted similarly for both systems. A similar order of magnitude of PCE loss has already been observed in the literature right after other types of glass–glass encapsulation processes [42]. The stability of the perovskite absorber under lamination was thus assumed considering a conservation of at least 80% of the initial performances after lamination. The explanation may lie in the small thermal degradation of the perovskite due to the applied 130 °C temperature during lamination and/or mechanical stress within the different layers constituting the PV stack. According to the lamination operating conditions, we can hypothesize that the mechanical stress experienced by devices with a flexible backsheet should be more homogeneous than that experienced by a rigid glass back cover. Indeed, the latter does not possess a spatial planarity guarantee and is also known to be subjected to potential glass warping when introducing a cold PV device within the preheated laminator. This could act on the FF, as observed, and on Voc. On the other hand, it is well known that polymer film allows for better heat dissipation than glass. This allows us to hypothesize greater thermal stress for perovskite during glass–glass encapsulation. This could act on Jsc, as observed, and again on Voc.

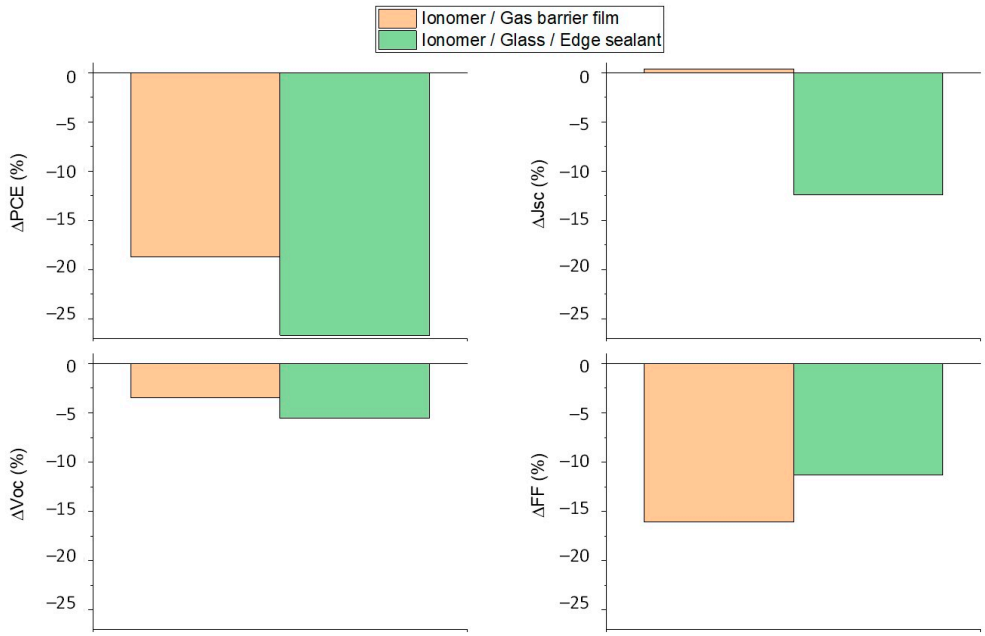

Figure 3. Impact of glass–backsheet (orange) and glass–glass (green) encapsulation processes on the photovoltaic parameters of c-PSC devices: percentage of variation for PCE, Jsc, Voc and FF between, after and before encapsulation.

3.2. Aging of c-PSC Encapsulating Devices

3.2.1. Evolution of Photovoltaic Performances and Parameters

To evaluate the relevance of encapsulating our c-PSC devices, an evaluation of the lifetime of non-encapsulated cells was first made under 85 °C/45% RH stress conditions. Open cells were dead before 10 h of exposition, highlighting the need for a pertinent encapsulation (under stronger 85 °C/85% RH conditions, cells were even non-functional after less than one hour of exposure). It should be interesting to add that cells protected by a non-sealed glass (with a piece of glass just laid on the PV cell) are fully dead after 500 h at 85 °C/45% RH conditions, with a PCE reduced to half after 200 h. The latter result is close to the one obtained with previously reported defective glass–glass devices without PIB at 85 °C/85% RH conditions (Figure S2).

Figure 4 presents the evolution of normalized photovoltaic parameters for c-PSC devices encapsulated using the two selected systems: glass–backsheet (i.e., ionomer/gas barrier film) and glass–glass (i.e., ionomer/glass/edge sealant). A sample of the evolution of the J–V curves is shown in Figure S3, together with the aging campaigns' initial average electrical parameters values in Table S1. In Figure 4a, the devices were exposed to DH conditions: 85 °C/85% RH under air. Glass–glass encapsulation upgraded using PIB edge sealant was then effective against external atmosphere permeation and ensured an increased stability when compared with either non-encapsulated devices or the original glass–glass encapsulation presented in Figure S2. The glass–backsheet encapsulation presents a very close efficacy to the glass–glass + PIB encapsulation, and slightly better toward the end of the aging. Surprisingly, although significantly lower moisture ingress might be expected for the cells including edge sealant due to its favorable WVTR [43], this was not the case here. Figure 4b presents the aging of identical encapsulated devices exposed only to a temperature (T) condition: 85 °C under nitrogen. This additional "T" aging allowed us to confirm that the decrease in performance observed upon "DH" was not due to potential damages endured during lamination but to the effect of moisture/oxygen ingress after their progressive permeation through the encapsulation. Indeed, upon "T" aging, both devices were very stable, with PV performance levels being maintained for up to 2500 h with PCE losses lower than 20% in absolute. This time, again, glass–backsheet encapsulation presented slightly better stability than glass–glass + PIB encapsulation, however with closely similar behavior.

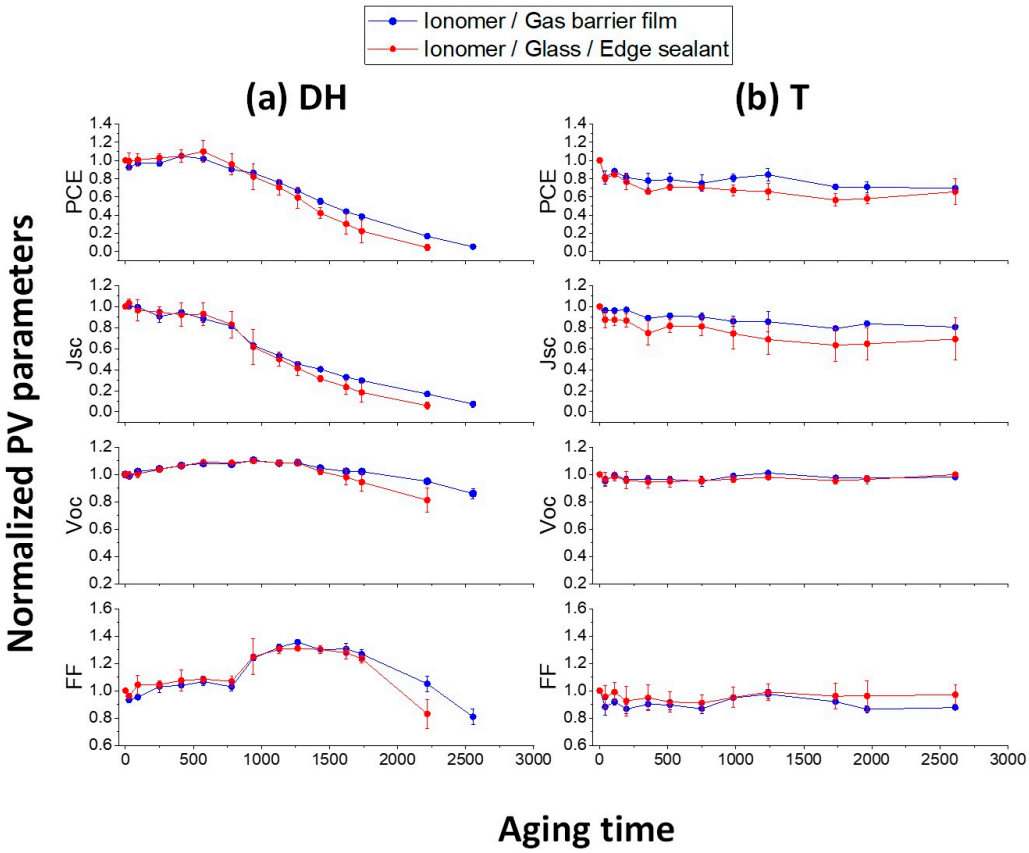

Figure 4. Evolution of the photovoltaic parameters for the encapsulated devices exposed either to (**a**) damp-heat (DH) or to (**b**) temperature under nitrogen (T) conditions.

The analysis of PCE together with other PV parameters (Jsc, Voc and FF) presented in Figure 4 allows to propose the following hypothetical degradation mechanism. Specific characterizations will then be conducted in the following sections to confirm the origin of flaws and degradations using light-beam-induced current mapping, impedance spectroscopy, photoluminescence imaging and a specifically developed image processing technique using partial device aging.

First, the sole temperature parameter (T aging) causes a slight degradation of the perovskite leading to a PCE reduction of 20% in absolute within ~500 h. This is mainly related to Jsc deterioration, which can be found in both DH and T aging. However, the macroscopic PCE of the cells exposed to DH experienced a close-to-10% relative increase for up to 600 h. It thus seems that both encapsulations allow for the passage of small contents of moisture and/or oxygen right at the beginning of aging campaigns, leading to an initial PCE improvement related to a rise in Voc. This could be due to a small "maturation" phenomenon [11] occurring in parallel with perovskite degradation upon temperature at the first stage of aging even under the strong DH conditions. Indeed, in situ passivation of perovskite defects at grain boundaries using a small amount of PbI_2 is known to be able to enhance both Voc and FF [44]. In accordance with the Voc increase, the FF parameter also drastically increases after 1000 h of DH aging while remaining constant throughout T aging.

Regarding the Jsc decrease during the first 500 h of both T and DH aging, it could either be caused by the high temperature itself or by an interaction with the encapsulation polymers and gases trapped within them prior to the lamination. It has also been reported that perovskite films under tensile stress are more prone to cracking and delamination [45]. However, in the presence of a small amount of moisture for DH, defects within the perovskite absorber are passivated, causing a Voc improvement, which anticipates the Jsc impact on the PCE.

Later, when higher levels of moisture penetrate the samples (in combination with the high temperature at around 1000 h of DH aging), this leads to a significant degradation of the perovskite absorber, which is reflected by all the photovoltaic parameters. Until 1500 h, the degradation of the other layers within the cells should not be considered, as Voc and FF remain constant and degrade severely only after detrimental deterioration of the Jsc for the DH aging.

To conclude, both selected encapsulations slow down the degradation of c-PSC devices in a more effective way than our previously reported ionomer edge sealing method [11]. When similar c-PSC processing methods were used, the latter led to a drastic loss of PV performance after 200 h of DH with all cells fully degraded after 1000 h, while, here, performances were maintained under a 20% loss for at least 1000 h under DH conditions. As the performance durability with the glass–glass + PIB encapsulation concept was slightly lower than with the glass–backsheet encapsulation, further investigation is needed in order to elucidate the potential impact on performance durability of either the initial stress during lamination or the strength of the encapsulation system itself.

3.2.2. LBIC Mapping

To investigate the spatial distribution of the defects, LBIC mapping was performed on the devices. This furnishes a localization of the degradation signs (see representative sampling presented in Figure 5). A statistical distribution using box plots is also represented in Figure S4, with more sampling points. First, LBIC maps at T0 are homogeneous, highlighting a good homogeneity of the inkjet process used without significant damage due to the lamination process. The slight disparity in average Isc at T0 between Figure 5a and b is lower than 10% and is due to the use of a different batch.

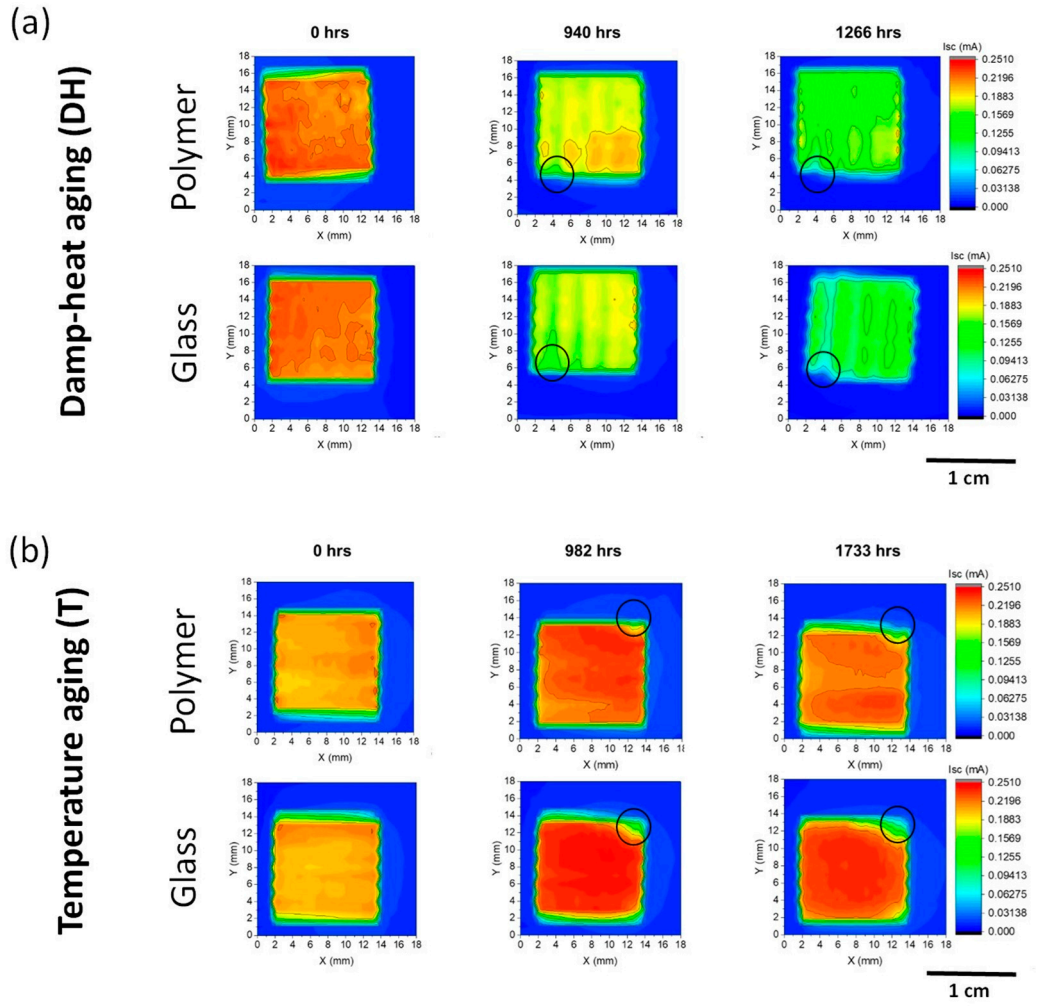

Figure 5. LBIC maps at different aging times for (**a**) damp-heat (DH) exposure and (**b**) temperature (T) exposure with either the ionomer/gas barrier film or the ionomer/glass/edge sealant encapsulations (black circles highlight reproducible defaults within the same batch).

The initial improvement in the PCE properties observed with J–V measurements during DH aging appears here as a slight LBIC-Isc increase during the first 400–500 h (see Figure S4). This is not correlated with an increase in the macroscopic Jsc during J–V measurements. However, as the intensity of the excitation signal is quantitatively lower using LBIC, it can highlight small phenomena that are not visible using J–V. Then, a progressive significant decrease in the LBIC-Isc was observed, which is compatible with the macroscopic Jsc decrease after 500 h in DH aging. With aging time, some edge defects could be noticed, providing local areas with LBIC-Isc = 0 mA (see black circles). They were surprisingly always located at the same spot within the same batch (i.e., bottom left for Figure 5a and top right for Figure 5b) and were present in both T and DH aging. It could probably be related to a defect in the encapsulation process: either a non-optimized adhesion of sealant resulting in a preferential access path for oxygen and moisture, or more pronounced mechanical stress generated during the lamination process revealed after aging. Except for this isolated defect, the decrease in LBIC-Isc was homogeneous within the entire device surface. This means that the diffusion of the water molecules within the sealing ionomer is faster than their reaction with the perovskite material. A particular pattern with vertical lines can, however, be noticed for samples exposed to DH aging. The lines with higher Isc values are related to the movement of the inkjet printer head where perovskite is deposited, and the lines with lower Isc values are related to the perovskite areas filled by diffusion through the mesoporous layers. This probably highlights a lower

quantity of perovskite in the latter. Regarding the samples aged only thermally (T), a small increase in Isc till 1000 h followed by a slight decrease after 1000 h was observed, but it was not significant.

3.2.3. Impedance Spectroscopy

Impedance spectroscopy measurements can be useful for the identification of the different degradation mechanisms involved in the performance reduction of the studied devices. Typical Nyquist plot patterns of both unaged and aged devices are illustrated in Figure 6a,b. A sampling of obtained plots during DH and T aging for both selected glass–backsheet and glass–glass encapsulations are also represented in Figure S5 in the Supplementary Materials File.

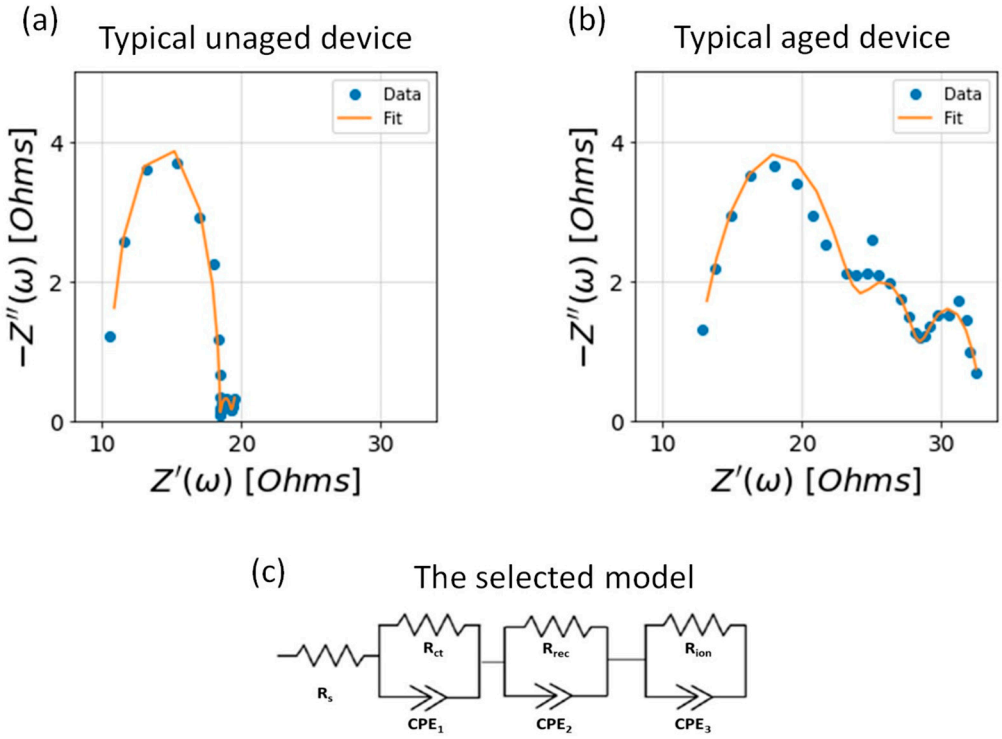

Figure 6. Typical Nyquist plots obtained from impedance measurements for (**a**) unaged devices and (**b**) aged devices; (**c**) the 3-RC model used for fitting the Nyquist plots obtained during aging campaigns.

It can be observed that the ion diffusion, probably due to perovskite decomposition, appeared as an increased semi-infinite impedance for both types of aging. Figure 6c presents the 3-RC model used for fitting all the here-obtained Nyquist plots [35]. This model is one of the most proposed to fit c-PSC device architectures without a hole transporting layer as is the case here, providing the extraction of the series resistance (Rs), geometrical resistance (Rct) and recombination resistance (Rrec). These extracted parameters are presented in Figure 7 for glass–backsheet encapsulated devices. A similar behavior was found with glass–glass encapsulated devices, as presented in Figure S6 in Supplementary Materials. Another represented significant parameter is the ideality factor of the first semicircle, which was calculated as described in the experimental section and indicates the change in the lattice of the perovskite absorber when it is lower than one [36].

Figure 7 presents the evolution of the described parameters in cells exposed either to DH or T conditions. For the DH-aged samples (black symbols), the Rs increased after up to 600 h of exposure and then decreased for the rest of the experiment. A reasonable explanation is that the electrical contact between the perovskite-filled mesoporous bulk structure and the electrodes is deteriorating due to the initial decomposition of the perovskite layer caused by heat exposure. The trend then changed toward the opposite direction after a

significant amount of moisture penetrated the encapsulation, which can be explained as the passivation of perovskite defaults via a small amount of PbI_2 degradation byproduct, before increasing again when the degradation level increased. Moreover, Rct and Rrec reached elevated values with aging due to the gradual decomposition of the perovskite absorber and the passivation effect of moisture, respectively. In addition, changes caused by humidity on the lattice of the bulk of the cell are visible in the ideality factor evolution, which dropped significantly after 600 h of DH exposure. It should be noted that most of the parameters displayed for the last DH aging point did not follow the previous evolution, but they are probably not correct due to a miscalculation of values related to a degraded Nyquist plot.

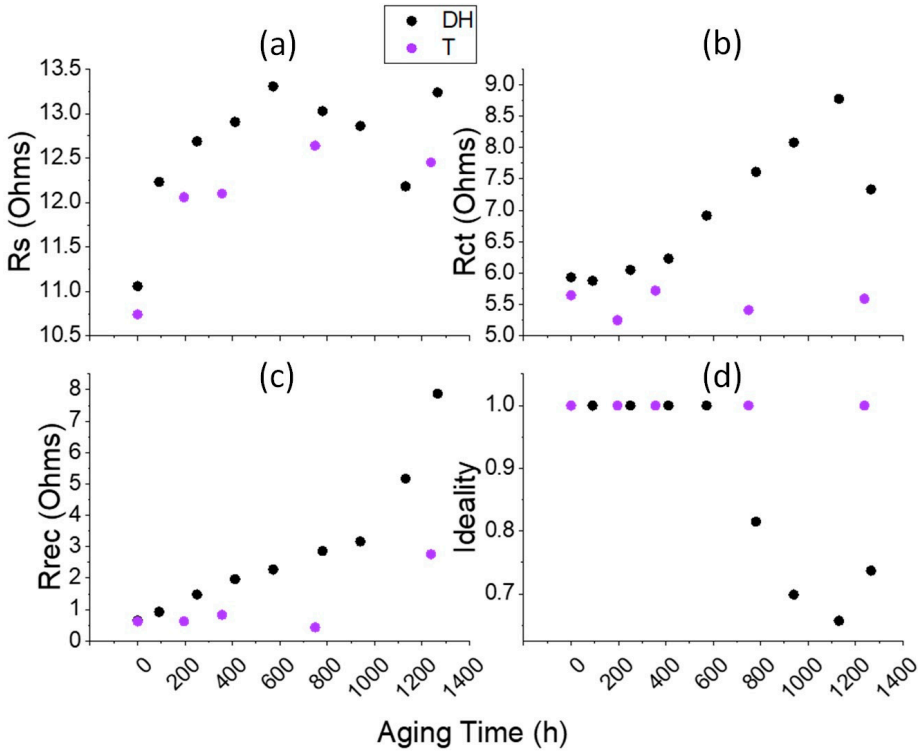

Figure 7. Evolution of parameters extracted from impedance spectroscopy measurements: (**a**) Rs; (**b**) Rct; (**c**) Rrec and (**d**) ideality factor for glass–backsheet encapsulated c-PSC devices during damp-heat (DH) and temperature under nitrogen (T) aging campaigns (parameters of evolution for glass–glass encapsulated c-PSC devices are similar, as presented in Figure S6).

Regarding T aging (purple points), Rs also increased with aging time, which is compatible with the observed Jsc decrease measured in J–V. In other words, the degradation of the contact between the perovskite layer and the electrodes was mainly responsible for the loss in current. In contrast, Rct and Rrec were not much altered, suggesting that no passivation occurred in the absence of moisture/oxygen and that the degradation essentially occurred at the perovskite interfaces. Additionally, the value of the ideality factor remained equal to 1 for the duration of the T aging.

3.2.4. PL Imaging

To further evaluate the quality and potential degradation of the perovskite absorber, the full PV devices were regularly characterized by photoluminescence imaging while aging either in DH or in T conditions. A sampling of images obtained from the TiO_2 side is presented in Figure 8 for both types of encapsulation.

One can easily observe the significant increase in the perovskite layer photoluminescence during DH aging, while the photoluminescence slightly decreased during T aging. In addition, for DH, a statistical appearance of local defaults (points) with higher photo-

luminescence was gradually observed and, at about 1000 h, the same particular pattern as the one highlighted with LBIC characterization is present (vertical lines). This again highlights a smaller amount of perovskite outside the path of the inkjet printer head, where the increase in the default amount due to moisture penetration is more noticeable on the PL signal. Concerning the local default observed with LBIC mapping for all devices during both aging campaigns (highlighted by black circles in Figure 5), it was not observable on the photoluminescence emission of perovskite. This means that their origin is not due to a more pronounced quantity of moisture/oxygen on the border of the devices, but more probably to more pronounced mechanical stress generated at interfaces during the lamination process and revealed during aging. Finally, when the photoluminescence drastically rises, the observed light image with a hatching pattern as at 1266 h is in fact synonymous with the saturation of the camera detector.

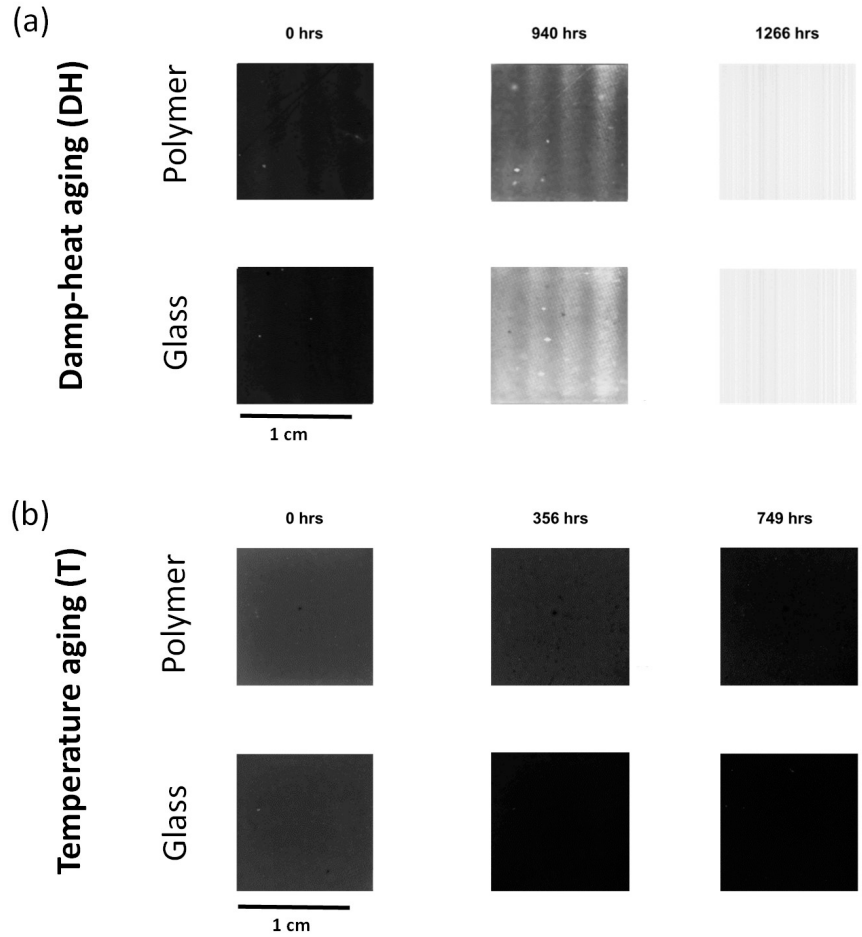

Figure 8. PL images at different aging times for (**a**) damp-heat (DH) exposure and (**b**) temperature (T) exposure with either the glass–backsheet or the glass–glass encapsulations.

For better quantification throughout the aging processes, the average grey level values are represented in Figure 9 during DH and T aging processes for both encapsulation types (according to the grey scale, 0 being for black and 255 for white). The observed increase of PL occurred regularly for both encapsulated c-PSC structures until saturation of the camera detector occurred between 1000 and 1500 h. Then, the PL intensity decreased. This is in agreement with observations described in the literature [46]. Indeed, the initial PL increase should be more related to passivation via PbI_2 formation (explaining the initial improvement of the Voc), and the PL decrease is more related to an important degradation of the perovskite material [47]. In contrast, no increase in the PL intensity was observed after pure T aging. The gradual slight homogeneous reduction in the PL signal is probably related to the gradual amorphization of the absorber without PbI_2 passivation in the

absence of oxygen and moisture, as T aging is conducted under an inert atmosphere (i.e., under nitrogen). This phenomenon directly explains the resulting slight reduction in the macroscopic Jsc.

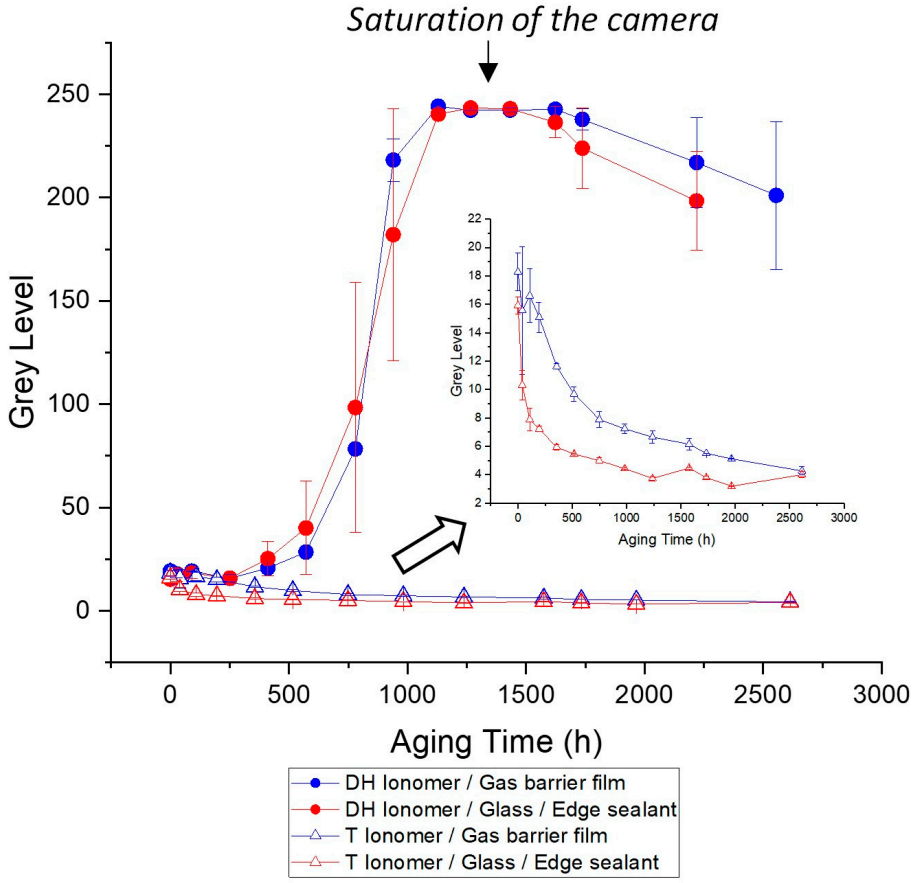

Figure 9. Extracted grey level evolution from the PL images of the cells aged under damp-heat (DH) or temperature (T) conditions. (Enlargement = zoom for aging with temperature (T)).

3.2.5. Area and Thickness Evolution of the Perovskite Layer

According to a previously reported machine learning imaging technique [39,40], it was possible to estimate both the thickness of the perovskite material and the perovskite-filled area evolutions during aging. Figure 10a presents a typical example of the acquired photographs, and Figure 10b shows the resulting maps obtained after image processing. For this purpose, partial devices without the final black carbon layer were used in order to be able to detect the color related to perovskite. The perovskite layer lightens as it ages, changing from dark brown at T0 (for perovskite) to light yellow at the end of aging under DH conditions (for the PbI_2 degradation byproduct).

With the use of complete devices with carbon electrodes, the color change of perovskite was only detectable for much-degraded devices with visible penetration of water, as illustrated in Figure S2a for a glass–glass encapsulation without PIB. For the encapsulation concepts selected here, no major color change was observable even at the end of aging. It should be mentioned that the perovskite layer is thick and constitutes a conductive path within a ZrO_2-insulating mesoporous scaffold (1 µm thickness). According to impedance spectroscopy characterization, the degradation of the contact between the perovskite layer and the electrodes is mainly responsible for the loss in current. Thus, a small degradation amount within the perovskite layer (amorphization with or without PbI_2 byproduct) can lead to non-functional cells. If a small change within the perovskite layer color occurs, it will be hidden by the carbon electrode darkness.

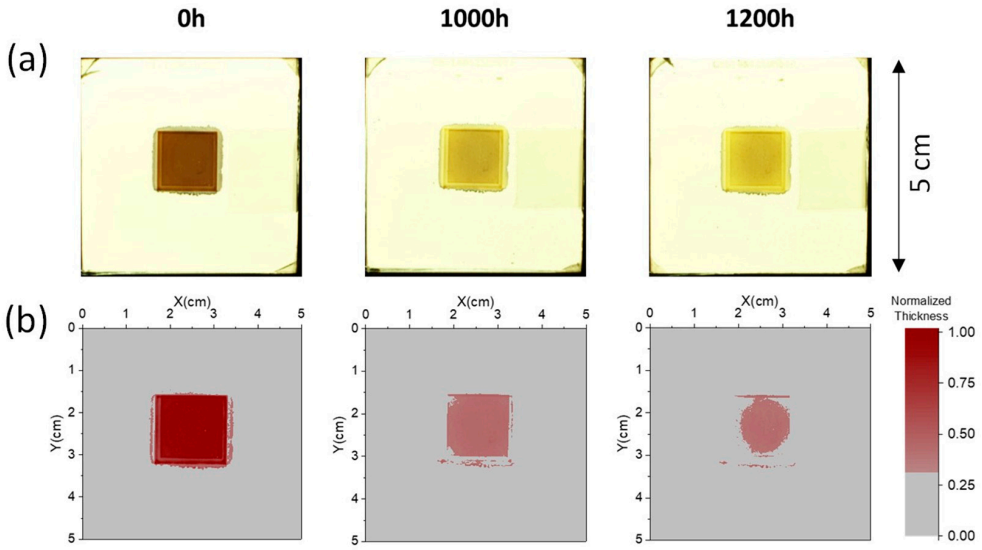

Figure 10. Examples of (**a**) top view photographs and (**b**) respective thickness maps obtained after processing (for devices without carbon layer, aged under DH conditions with a glass-backsheet encapsulation).

On the thickness maps, the grey color represents the absence of perovskite, while the color gradient from light to dark red expresses an increase in perovskite absorber thickness. The deterioration of the area filled by perovskite and the reduction of the perovskite thickness with aging time are thus both visible in Figure 10b.

First, partial stacks without the opaque carbon layer, i.e., "Glass/TiO_2/ZrO_2 + Perovskite" as presented in Figure 11a were studied. Partial stacks were encapsulated using the same procedure as for the full PV devices and exposed to DH conditions. The area and thickness of perovskite were extracted for all the studied samples from maps similar to those presented in Figure 10, which illustrate the results obtained with glass–backsheet encapsulation.

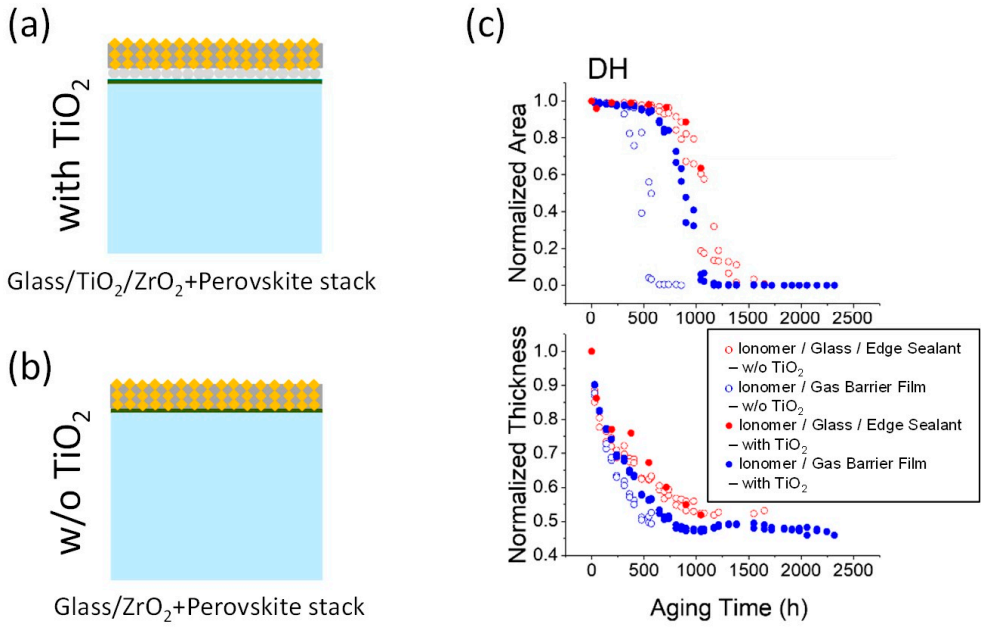

Figure 11. Architectures of the studied partial devices without opaque carbon layer: (**a**) stack without carbon and with TiO_2, and (**b**) stack without carbon and without TiO_2; (**c**) normalized areas and average thicknesses corresponding to the perovskite material during damp-heat (DH) aging campaign for the two encapsulation types and for both partial stacks represented in (**a**,**b**).

We can observe a particular "round" pattern around 1000 h of DH aging. This is a novelty compared with other imaging techniques previously presented (LBIC and PL). As partial devices do not contain the thick 12-µm mesoporous carbon layer, we can conclude that the latter was previously protecting the full PV devices by delaying and homogenizing the moisture diffusion toward the perovskite layer. As presented in Figure 11c (full symbols), it is obvious that the durability of the partial stacks "Glass/TiO_2/ZrO_2 + Perovskite" is significantly reduced compared with full PV devices "Glass/TiO_2/ZrO_2 + Perovskite/Carbon". For full PV devices, the PCE loss is lower than 20% in absolute after 1000 h at DH aging for both glass–backsheet and glass–glass encapsulations. Here, without the carbon layer, the perovskite layer was already at half thickness at 700 h and 1000 h for glass–backsheet and glass–glass encapsulations, respectively, together with the ignition of a drastic fall of the area filled by perovskite. According to the literature [48], carbon is known to be hydrophobic and thus to be able to protect the perovskite layer from moisture, which is here evidenced by the difference in behavior between full-device LBIC and PL mapping and partial-device image processing maps.

To go further, additional partial stacks without carbon and without TiO_2 were also prepared (i.e., "Glass/ZrO_2 + Perovskite" as presented in Figure 11b). Once again, we can observe that TiO_2 also plays a protective role against moisture diffusion. As presented in Figure 11c, open symbols present faster degradation than their related full symbols. This even highlights faster degradation for glass–backsheet (i.e., glass–ionomer–gas barrier film) encapsulated devices than for glass–glass (i.e., glass–ionomer–glass with PIB edge sealant) ones. With the PIB edge sealant together with the glass rear cover protection, the presence or absence of TiO_2 did not affect much the degradation kinetics. But, in the case of glass–backsheet encapsulation, the drastic fall of the area filled by perovskite occurs after 300 h without TiO_2 vs. 700 h with TiO_2. The perovskite thickness decrease also presents a steeper slope without TiO_2.

According to their WVTR values, the ionomer water vapor permeation is 1.9 $g/m^2/day$ vs. 0.12 $g/m^2/day$ for the PIB edge sealant. With the latter only being used in the case of glass–glass encapsulation, it could be assumed to offer about 10 times better edge protection for the final glass–glass encapsulation. However, this is probably overstated, according to the potential bad adhesion of the ionomer sealant present after the 0.5 cm width of PIB. Regarding the surface protection, it again seems that glass–glass should be more effective than glass–backsheet with full protection while using glass against a permeation lower than 5×10^{-4} $g/m^2/day$, but non-equal to zero, occurring for the polymer backsheet. However, although glass–glass encapsulation with PIB edge-sealant is shown in this section to be more effective in terms of moisture/oxygen ingress, the obtained difference is not reflected in the PCE durability under the same DH aging condition (see Table 2). It thus seems that the c-PSC device architecture itself also plays an important role in slowing down water diffusion, especially with TiO_2 and carbon layers. This finally leads to the quite equivalent durability of both studied systems, even if, in terms of WVTR, the PIB edge-sealant is more efficient than the used ionomer, and glass is more protective than the barrier polymer used as backsheet. According to the literature, other materials are currently being studied in order to increase the barrier properties of traditional encapsulating materials (for instance, multi-walled carbon nanotubes as an additive in epoxy resin [49] or graphene layers co-laminated with polymers [50]). A non-negligible advantage in our study is that TiO_2 and carbon are quite cheap materials that also participate in the photovoltaic conversion themselves while delaying the moisture ingress.

On another note, according to the PCE evolution with either T or DH aging campaigns (see Table 2), it seems that the glass–backsheet encapsulation system can finally lead to slightly more durable devices. One possible reason could originate in the difference in the lamination stress. Indeed, even if applied lamination conditions are identical, the difference in rigidity of the two studied configurations can result in a different thermomechanical constraint within the c-PSC devices [45]. This could lead to different degradation pathways

and is compatible with the more impacted initial PCE value for devices with glass–glass encapsulation.

Table 2. Photovoltaic parameters for glass–glass and glass–backsheet devices at the end of aging campaigns for both "DH" and "T" conditions.

	PCE (%)	Jsc (mA/cm^2)	Voc (V)	FF
Ionomer/Gas barrier film DH 2200 h	1.73	4.01	0.885	0.49
Standard Deviation	±0.13	±0.15	±0.015	±0.03
Ionomer/Glass/Edge sealant DH 2200 h	0.44	1.23	0.753	0.41
Standard Deviation	±0.31	±0.69	±0.079	±0.06
Ionomer/Gas barrier film T 2600 h	7.36	19.63	0.915	0.41
Standard Deviation	±0.13	±0.11	±0.008	±0.01
Ionomer/Glass/Edge sealant T 2600 h	6.41	15.03	0.931	0.47
Standard Deviation	±1.88	±5.19	±0.006	±0.02

4. Conclusions

The aim of the work presented was to compare the efficiency of glass–glass and glass–backsheet encapsulations for the application of carbon-based perovskite solar cells, which have great potential for industrialization. This was conducted by first separating the relative effect of humidity and heat. A time evolution of the macroscopic PCE was performed together with specific characterizations in order to scout the origin of flaws and degradations. After an update of the glass–glass encapsulation with an additional PIB edge-sealant in order to prevent the occurrence of observed adhesion flaws, both encapsulation systems surprisingly provide a similar impact on performance durability. Sole temperature stress (T) caused a two-step degradation which was rapid during the first 48 h and then more moderated. The addition of water and oxygen stresses to temperature led to an initial passivation of defects within the perovskite, which improved the photovoltaic efficiency of the cells during the first 500 h of DH aging, before becoming prejudicial after 1000 h. The IEC requirement for the DH test is 1000 h (IEC 61215-1:2021 [51] is the effective updated last version), and very few studies present data after 1000 h of aging. As our samples demonstrated a conservation of at least 80% of initial performances (T80) after 1000 h under DH conditions, we can thus validate our systems. A significant additional contribution of the paper is the identification of both TiO_2 and carbon layers as barriers against moisture permeation, which inhibit moisture paths through the interfaces. This is the origin of equivalent durability for the two studied systems, even though glass–backsheet encapsulation has proved to be less effective than glass–glass encapsulation at protecting perovskite from aging via DH when no TiO_2 or carbon layer is used. It could thus be interesting to study the protective role of other types of transporting layers with the incremental procedure developed in this paper, together with studying the moisture protective role for TiO_2, carbon and our developed encapsulations in various other perovskite formulations.

Supplementary Materials: The following supporting information can be downloaded at: https://www.mdpi.com/article/10.3390/pr11092742/s1, Table S1: Impact of encapsulation processes on the photovoltaic parameters of c-PSC devices: average values for PCE, Jsc, Voc and FF after the two selected encapsulations (To values for aging campaigns); Figure S1: Encapsulation procedure; Figure S2: Illustration for the adherence problem of the ionomer film on the glass substrate; Figure S3: Examples of typical J–V curves measured for the same devices before and after lamination, and sampling during the aging campaigns; Figure S4: LBIC mapping distributions (box-plots) during aging; Figure S5: Typical Nyquist plots during damp-heat (DH) and thermal (T) aging; Figure S6: Evolution of parameters extracted from impedance spectroscopy measurements for devices with "ionomer and glass–glass + PIB" encapsulation.

Author Contributions: Conceptualization, S.C., D.M. and N.K.; methodology, S.C., D.M., N.K., L.P., E.P. and L.F.; validation, N.K. and D.M.; formal analysis, N.K., D.M., L.P., E.P., L.F. and S.C.; investigation, N.K., C.F. and D.M.; writing—original draft preparation, N.K. and L.P.; writing—review and editing, S.C., D.M., E.P., L.F., L.W. and K.S. All authors have read and agreed to the published version of the manuscript.

Funding: This study has received funding from the European Solar Eranet program UNIQUE under grant agreement No. ANR-19-SOL2-0004-03 regarding the French funding. Additional funding is received by the project PROPER supported by "EIG Concert Japan" and financed from the French National Centre for Scientific Research under the funding number "IRUEC 222437".

Data Availability Statement: The data presented in this study are available on request from the corresponding author.

Conflicts of Interest: The authors declare no conflict of interest.

References

1. NREL. Best Research-Cell Efficiency Chart. Available online: https://www.nrel.gov/pv/cell-efficiency.html (accessed on 21 July 2023).
2. Kim, H.-S.; Lee, C.-R.; Im, J.-H.; Lee, K.-B.; Moehl, T.; Marchioro, A.; Moon, S.-J.; Humphry-Baker, R.; Yum, J.-H.; Moser, J.E.; et al. Lead Iodide Perovskite Sensitized All-Solid-State Submicron Thin Film Mesoscopic Solar Cell with Efficiency Exceeding 9%. *Sci. Rep.* **2012**, *2*, 591. [CrossRef] [PubMed]
3. Han, Y.; Meyer, S.; Dkhissi, Y.; Weber, K.; Pringle, J.M.; Bach, U.; Spiccia, L.; Cheng, Y.-B. Degradation Observations of Encapsulated Planar $CH_3NH_3PbI_3$ Perovskite Solar Cells at High Temperatures and Humidity. *J. Mater. Chem. A* **2015**, *3*, 8139–8147. [CrossRef]
4. Burschka, J.; Pellet, N.; Moon, S.-J.; Humphry-Baker, R.; Gao, P.; Nazeeruddin, M.K.; Grätzel, M. Sequential Deposition as a Route to High-Performance Perovskite-Sensitized Solar Cells. *Nature* **2013**, *499*, 316–319. [CrossRef] [PubMed]
5. Zheng, H.; Liu, G.; Zhang, C.; Zhu, L.; Alsaedi, A.; Hayat, T.; Pan, X.; Dai, S. The Influence of Perovskite Layer and Hole Transport Material on the Temperature Stability about Perovskite Solar Cells. *Sol. Energy* **2018**, *159*, 914–919. [CrossRef]
6. Kobayashi, E.; Tsuji, R.; Martineau, D.; Hinsch, A.; Ito, S. Light-Induced Performance Increase of Carbon-Based Perovskite Solar Module for 20-Year Stability. *Cell Rep. Phys. Sci.* **2021**, *2*, 100648. [CrossRef]
7. Emery, Q.; Remec, M.; Paramasivam, G.; Janke, S.; Dagar, J.; Ulbrich, C.; Schlatmann, R.; Stannowski, B.; Unger, E.; Khenkin, M. Encapsulation and Outdoor Testing of Perovskite Solar Cells: Comparing Industrially Relevant Process with a Simplified Lab Procedure. *ACS Appl. Mater. Interfaces* **2022**, *14*, 5159–5167. [CrossRef]
8. Mei, A.; Li, X.; Liu, L.; Ku, Z.; Liu, T.; Rong, Y.; Xu, M.; Hu, M.; Chen, J.; Yang, Y.; et al. A Hole-Conductor-Free, Fully Printable Mesoscopic Perovskite Solar Cell with High Stability. *Science* **2014**, *345*, 295–298. [CrossRef]
9. Fagiolari, L.; Bella, F. Carbon-Based Materials for Stable, Cheaper and Large-Scale Processable Perovskite Solar Cells. *Energy Environ. Sci.* **2019**, *12*, 3437–3472. [CrossRef]
10. Zouhair, S.; Yoo, S.; Bogachuk, D.; Herterich, J.P.; Lim, J.; Kanda, H.; Son, B.; Yun, H.J.; Würfel, U.; Chahboun, A.; et al. Employing 2D-Perovskite as an Electron Blocking Layer in Highly Efficient (18.5%) Perovskite Solar Cells with Printable Low Temperature Carbon Electrode. *Adv. Energy Mater.* **2022**, *12*, 2200837. [CrossRef]
11. Perrin, L.; Flandin, L.; Farha, C.; Narbey, S.; Martineau, D.; Planès, E. Investigation of Post-Treatment Improving Perovskite Solar Cells Initial Performances and Study of Its Impact on the Durability. *Energies* **2023**, *16*, 5254. [CrossRef]
12. Bai, Y.; Mora-Seró, I.; De Angelis, F.; Bisquert, J.; Wang, P. Titanium Dioxide Nanomaterials for Photovoltaic Applications. *Chem. Rev.* **2014**, *114*, 10095–10130. [CrossRef]
13. Gusmano, G.; Montesperelli, G.; Rapone, M.; Padeletti, G.; Cusmà, A.; Kaciulis, S.; Mezzi, A.; Maggio, R.D. Zirconia Primers for Corrosion Resistant Coatings. *Surf. Coat. Technol.* **2007**, *201*, 5822–5828. [CrossRef]
14. Rao, M.K.; Sangeetha, D.N.; Selvakumar, M.; Sudhakar, Y.N.; Mahesha, M.G. Review on Persistent Challenges of Perovskite Solar Cells' Stability. *Sol. Energy* **2021**, *218*, 469–491. [CrossRef]
15. Pradid, P.; Sanglee, K.; Thongprong, N.; Chuangchote, S. Carbon Electrodes in Perovskite Photovoltaics. *Materials* **2021**, *14*, 5989. [CrossRef] [PubMed]
16. Mei, A.; Sheng, Y.; Ming, Y.; Hu, Y.; Rong, Y.; Zhang, W.; Luo, S.; Na, G.; Tian, C.; Hou, X.; et al. Stabilizing Perovskite Solar Cells to IEC61215:2016 Standards with over 9000-h Operational Tracking. *Joule* **2020**, *4*, 2646–2660. [CrossRef]
17. Huang, T.; Tan, S.; Yang, Y. Material, Phase, and Interface Stability of Photovoltaic Perovskite: A Perspective. *J. Phys. Chem. C* **2021**, *125*, 19088–19096. [CrossRef]
18. Kundu, S.; Kelly, T.L. In Situ Studies of the Degradation Mechanisms of Perovskite Solar Cells. *EcoMat* **2020**, *2*, e12025. [CrossRef]
19. Aitola, K.; Gava Sonai, G.; Markkanen, M.; Jaqueline Kaschuk, J.; Hou, X.; Miettunen, K.; Lund, P.D. Encapsulation of Commercial and Emerging Solar Cells with Focus on Perovskite Solar Cells. *Sol. Energy* **2022**, *237*, 264–283. [CrossRef]

20. Fu, Z.; Xu, M.; Sheng, Y.; Yan, Z.; Meng, J.; Tong, C.; Li, D.; Wan, Z.; Ming, Y.; Mei, A.; et al. Encapsulation of Printable Mesoscopic Perovskite Solar Cells Enables High Temperature and Long-Term Outdoor Stability. *Adv. Funct. Mater.* **2019**, *29*, 1809129. [CrossRef]
21. Shi, L.; Young, T.L.; Kim, J.; Sheng, Y.; Wang, L.; Chen, Y.; Feng, Z.; Keevers, M.J.; Hao, X.; Verlinden, P.J.; et al. Accelerated Lifetime Testing of Organic–Inorganic Perovskite Solar Cells Encapsulated by Polyisobutylene. *ACS Appl. Mater. Interfaces* **2017**, *9*, 25073–25081. [CrossRef]
22. Cao, K.; Zuo, Z.; Cui, J.; Shen, Y.; Moehl, T.; Zakeeruddin, S.M.; Grätzel, M.; Wang, M. Efficient Screen Printed Perovskite Solar Cells Based on Mesoscopic $TiO_2/Al_2O_3/NiO$/Carbon Architecture. *Nano Energy* **2015**, *17*, 171–179. [CrossRef]
23. Martins, J.; Emami, S.; Madureira, R.; Mendes, J.; Ivanou, D.; Mendes, A. Novel Laser-Assisted Glass Frit Encapsulation for Long-Lifetime Perovskite Solar Cells. *J. Mater. Chem. A* **2020**, *8*, 20037–20046. [CrossRef]
24. Luo, Q.; Ma, H.; Zhang, Y.; Yin, X.; Yao, Z.; Wang, N.; Li, J.; Fan, S.; Jiang, K.; Lin, H. Cross-Stacked Superaligned Carbon Nanotube Electrodes for Efficient Hole Conductor-Free Perovskite Solar Cells. *J. Mater. Chem. A* **2016**, *4*, 5569–5577. [CrossRef]
25. Bella, F.; Griffini, G.; Correa-Baena, J.-P.; Saracco, G.; Gratzel, M.; Hagfeldt, A.; Turri, S.; Gerbaldi, C. Improving Efficiency and Stability of Perovskite Solar Cells with Photocurable Fluoropolymers. *Science* **2016**, *354*, 203–206. [CrossRef] [PubMed]
26. Pescetelli, S.; Agresti, A.; Viskadouros, G.; Razza, S.; Rogdakis, K.; Kalogerakis, I.; Spiliarotis, E.; Leonardi, E.; Mariani, P.; Sorbello, L.; et al. Integration of Two-Dimensional Materials-Based Perovskite Solar Panels into a Stand-Alone Solar Farm. *Nat. Energy* **2022**, *7*, 597–607. [CrossRef]
27. Li, J.; Xia, R.; Qi, W.; Zhou, X.; Cheng, J.; Chen, Y.; Hou, G.; Ding, Y.; Li, Y.; Zhao, Y.; et al. Encapsulation of Perovskite Solar Cells for Enhanced Stability: Structures, Materials and Characterization. *J. Power Sources* **2021**, *485*, 229313. [CrossRef]
28. Wang, Y.; Ahmad, I.; Leung, T.; Lin, J.; Chen, W.; Liu, F.; Ng, A.M.C.; Zhang, Y.; Djurišić, A.B. Encapsulation and Stability Testing of Perovskite Solar Cells for Real Life Applications. *ACS Mater. Au* **2022**, *2*, 215–236. [CrossRef] [PubMed]
29. Tracy, J.; Bosco, N.; Delgado, C.; Dauskardt, R. Durability of Ionomer Encapsulants in Photovoltaic Modules. *Sol. Energy Mater. Sol. Cells* **2020**, *208*, 110397. [CrossRef]
30. Wiesmeier, C.; Headrich, I.; Weiss, K.-A.; Duerr, I. Overview of PV Module Encapsulation Materials. *Photovolt. Int.* **2013**, *19*, 85–92.
31. Zhang, Y.; Xu, J.; Mao, J.; Tao, J.; Shen, H.; Chen, Y.; Feng, Z.; Verlinden, P.J.; Yang, P.; Chu, J. Long-Term Reliability of Silicon Wafer-Based Traditional Backsheet Modules and Double Glass Modules. *RSC Adv.* **2015**, *5*, 65768–65774. [CrossRef]
32. Slauch, I.M.; Vishwakarma, S.; Tracy, J.; Gambogi, W.; Meier, R.; Rahman, F.; Hartley, J.Y.; Bertoni, M.I. Manufacturing Induced Bending Stresses: Glass-Glass vs. Glass-Backsheet. In Proceedings of the 2021 IEEE 48th Photovoltaic Specialists Conference (PVSC), IEEE, Fort Lauderdale, FL, USA, 20 June 2021; pp. 1943–1948.
33. Singh, J.P.; Guo, S.; Peters, I.M.; Aberle, A.G.; Walsh, T.M. Comparison of Glass/Glass and Glass/Backsheet PV Modules Using Bifacial Silicon Solar Cells. *IEEE J. Photovolt.* **2015**, *5*, 783–791. [CrossRef]
34. Stefanelli, M.; Vesce, L.; Di Carlo, A. Upscaling of Carbon-Based Perovskite Solar Module. *Nanomaterials* **2023**, *13*, 313. [CrossRef] [PubMed]
35. Abdulrahim, S.M.; Ahmad, Z.; Bahadra, J.; Al-Thani, N.J. Electrochemical Impedance Spectroscopy Analysis of Hole Transporting Material Free Mesoporous and Planar Perovskite Solar Cells. *Nanomaterials* **2020**, *10*, 1635. [CrossRef]
36. von Hauff, E. Impedance Spectroscopy for Emerging Photovoltaics. *J. Phys. Chem. C* **2019**, *123*, 11329–11346. [CrossRef]
37. Getting Started with Impedance.Py. Available online: https://impedancepy.readthedocs.io/en/latest/getting-started.html (accessed on 21 July 2023).
38. PyPI Pillow 9.1.0. Available online: https://pypi.org/project/Pillow (accessed on 21 July 2023).
39. Booker, E.; Boutin, J.-B.; Roux, C.; Manceau, M.; Berson, S.; Cros, S. Perovskite Test: A High Throughput Method to Screen Ambient Encapsulation Conditions. *Energy Technol.* **2020**, *8*, 2000041. [CrossRef]
40. Taherimakhsousi, N.; Fievez, M.; MacLeod, B.P.; Booker, E.P.; Fayard, E.; Matheron, M.; Manceau, M.; Cros, S.; Berson, S.; Berlinguette, C.P. A Machine Vision Tool for Facilitating the Optimization of Large-Area Perovskite Photovoltaics. *NPJ Comput. Mater.* **2021**, *7*, 190. [CrossRef]
41. Lange, R.F.M.; Luo, Y.; Polo, R.; Zahnd, J. The Lamination of (Multi)Crystalline and Thin Film Based Photovoltaic Modules. *Prog. Photovolt. Res. Appl.* **2011**, *19*, 127–133. [CrossRef]
42. Ramasamy, E.; Karthikeyan, V.; Rameshkumar, K.; Veerappan, G. Glass-to-Glass Encapsulation with Ultraviolet Light Curable Epoxy Edge Sealing for Stable Perovskite Solar Cells. *Mater. Lett.* **2019**, *250*, 51–54. [CrossRef]
43. Kempe, M.D.; Nobles, D.L.; Postak, L.; Calderon, J.A. Moisture Ingress Prediction in Polyisobutylene-based Edge Seal with Molecular Sieve Desiccant. *Prog. Photovolt. Res. Appl.* **2018**, *26*, 93–101. [CrossRef]
44. Chen, Y.; Meng, Q.; Xiao, Y.; Zhang, X.; Sun, J.; Han, C.B.; Gao, H.; Zhang, Y.; Lu, Y.; Yan, H. Mechanism of PbI_2 in Situ Passivated Perovskite Films for Enhancing the Performance of Perovskite Solar Cells. *ACS Appl. Mater. Interfaces* **2019**, *11*, 44101–44108. [CrossRef]
45. Boyd, C.C.; Cheacharoen, R.; Leijtens, T.; McGehee, M.D. Understanding Degradation Mechanisms and Improving Stability of Perovskite Photovoltaics. *Chem. Rev.* **2019**, *119*, 3418–3451. [CrossRef]
46. Goetz, K.P.; Taylor, A.D.; Paulus, F.; Vaynzof, Y. Shining Light on the Photoluminescence Properties of Metal Halide Perovskites. *Adv. Funct. Mater.* **2020**, *30*, 1910004. [CrossRef]

47. Wagner, L.; Mundt, L.E.; Mathiazhagan, G.; Mundus, M.; Schubert, M.C.; Mastroianni, S.; Würfel, U.; Hinsch, A.; Glunz, S.W. Distinguishing Crystallization Stages and Their Influence on Quantum Efficiency during Perovskite Solar Cell Formation in Real-Time. *Sci. Rep.* **2017**, *7*, 14899. [CrossRef]
48. Tian, T.; Zhong, J.; Yang, M.; Feng, W.; Zhang, C.; Zhang, W.; Abdi, Y.; Wang, L.; Lei, B.; Wu, W. Interfacial Linkage and Carbon Encapsulation Enable Full Solution-Printed Perovskite Photovoltaics with Prolonged Lifespan. *Angew. Chem. Int. Ed.* **2021**, *60*, 23735–23742. [CrossRef] [PubMed]
49. Choi, J.-M.; Suko, H.; Kim, K.; Han, J.; Lee, S.; Matsuo, Y.; Maruyama, S.; Jeon, I.; Daiguji, H. Multi-Walled Carbon Nanotube-Assisted Encapsulation Approach for Stable Perovskite Solar Cells. *Molecules* **2021**, *26*, 5060. [CrossRef] [PubMed]
50. Runser, R.; Kodur, M.; Skaggs, J.H.; Cakan, D.N.; Foley, J.B.; Finn, M.; Fenning, D.P.; Lipomi, D.J. Stability of Perovskite Films Encapsulated in Single- and Multi-Layer Graphene Barriers. *ACS Appl. Energy Mater.* **2021**, *4*, 10314–10322. [CrossRef]
51. *IEC 61215-1:2021*; Terrestrial Photovoltaic (PV) Modules—Design Qualification and Type Approval. IEC Webstore: Geneva, Switzerland, 2021. Available online: https://webstore.iec.ch/publication/61345 (accessed on 10 September 2023).